

# The GLUEX Start Counter Detector

E. Pooser<sup>a,b</sup>, F. Barbosa<sup>a</sup>, W. Boeglin<sup>b,\*</sup>, C. Hutton<sup>a</sup>, M. Ito<sup>a</sup>, M. Kamel<sup>b</sup>, P. Khetarpal<sup>b</sup>, A. LLodra<sup>b</sup>, N. Sandoval<sup>a</sup>, S. Taylor<sup>a</sup>, C. Yero<sup>b</sup>, B. Zihlmann<sup>a</sup>

<sup>a</sup>*Thomas Jefferson National Accelerator Facility, Newport News, VA 23606, USA*

<sup>b</sup>*Florida International University, Miami, FL, 33199, USA*

---

## Abstract

The design, fabrication, calibration, and performance of the GLUEX Start Counter detector is described. The GLUEX experiment, staged in Hall D at the Thomas Jefferson National Accelerator Facility (TJNAF), primarily aims to study the rich spectrum of photo-produced mesons with unprecedented statistics. The coherent bremsstrahlung technique is implemented to produce a linearly polarized photon beam incident on a liquid H<sub>2</sub> target. A Start Counter detector was fabricated to properly identify the accelerator electron beam buckets and to provide accurate timing information. The Start Counter detector was designed to operate at photon intensities of up to  $10^8 \gamma/s$  in the coherent peak and provides a timing resolution of  $\approx 250$  ps thus providing successful identification of the electron beam buckets to more than 99% accuracy. Furthermore, the Start Counter detector provides excellent solid angle coverage,  $\sim 90\%$  of  $4\pi$  hermeticity, a high degree of segmentation for background rejection, and is utilized in the level 1 trigger for the experiment. It consists of a cylindrical array of 30 thin scintillators with pointed ends that bend towards the beam at the downstream end. Magnetic field insensitive silicon photomultiplier detectors were selected as the readout system.

*Keywords:* GLUEX, Flash 250 MHz ADC, F1 TDC, Plastic Scintillator, Silicon Photomultiplier, Multi-Pixel Photon Counter, Time of Flight, Trigger, Particle Identification, Polishing Scintillators

---

## 1. Design

### 1.1. Overview

In this section we discuss the details of the GLUEX Start Counter design. The general engineering specifics pertaining to the scintillators, support structure, detector readout system and electronics are discussed.

The Start Counter (ST) detector, seen in Fig. 1, surrounds a 30 cm long super cooled liquid H<sub>2</sub> target while providing  $\sim 90\%$  of  $4\pi$  solid angle coverage relative to the target center. The primary purpose of the ST detector is, in coincidence with the tagger, to properly identify the electron beam bucket associated with detected particles produced via linearly polarized photons incident on the target. It is designed to operate at tagged photon intensities of up to  $10^8 \gamma/s$  in the coherent peak.

---

\*Corresponding Author

Email address: [boeglinw@fiu.edu](mailto:boeglinw@fiu.edu) (W. Boeglin)

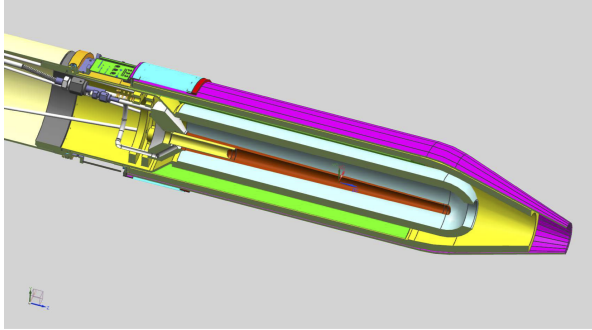


Figure 1: The GLUEX Start Counter mounted to the LH<sub>2</sub> target.

Moreover, the ST has a high degree of segmentation for background rejection, is utilized in particle identification, and is a primary component of the level 1 trigger of the GLUEX experiment during high luminosity running[1].

The ST detector consists of an array of 30 scintillators with pointed ends that bend towards the beam at the downstream end. EJ-200 scintilla-

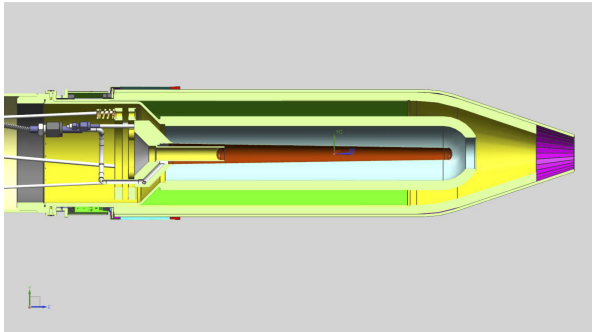


Figure 2: Cross section of the Start Counter detector mounted to the LH<sub>2</sub> target. The 30 cm target cell and scattering chamber is also shown.

tor material from Eljen Technology[2], which provides a decay time of 2.1 ns and a long attenuation length[3], was selected for this application. The amount of support structure material was kept to an absolute minimum in the active region of the detector and is made up of low density Rohacell[4]. Silicon Photomultiplier (SiPM) detectors were selected as the readout system. The detectors are not affected by the high magnetic field produced by the superconducting solenoid magnet. Moreover, the SiPMs were placed as close as possible to the upstream end of each scintillator element, thereby minimizing the loss of scintillation light[1].

### 1.2. Scintillator Paddles

Each individual paddle of the Start Counter was machined from a long, thin, polyvinyltoluene plastic EJ-200 scintillator bar that was diamond milled to be 600 mm in length, 3 mm thick, and  $20 \pm 2$  mm wide, by Eljen Technology. Each scintillator was bent around a highly polished aluminum drum by applying localized infrared heating to the bend region. The bent scintillator bars were then sent to McNeal Enterprises Inc.[5], a plastic fabrication company, where they were machined to the desired geometry illustrated in Fig. 3.

The paddles consist of three sections and are described from the upstream to the downstream end of the target. The straight section is 39.465 cm in length while being oriented parallel to both the target cell and beamline.. The bend region is a 18.5° arc of radius 120 cm and is downstream of the straight section. The tapered nose region is downstream of the target chamber and bends towards the beam line such that the tip of the nose is

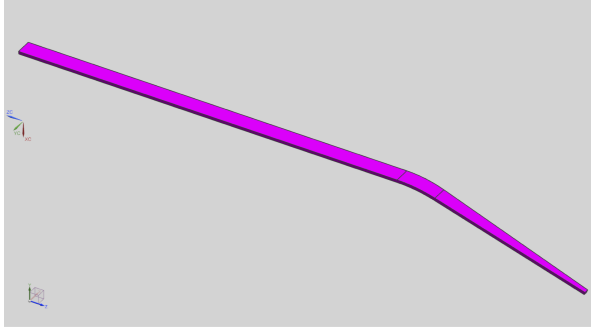


Figure 3: Start Counter single paddle geometry

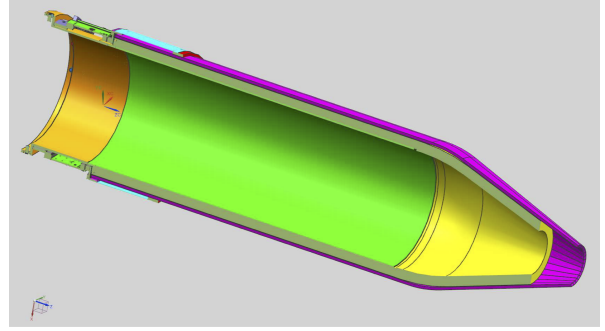


Figure 4: Cross section of the Start Counter detector

at a height of 2 cm above the beam line.

After the straight scintillator bar was bent to the desired geometry, the two flat surfaces that are oriented orthogonal to the wide, top and bottom, surfaces were cut at a  $6^\circ$  angle. During this process, the width of the top and bottom surfaces were machined to be 16.92 mm and 16.29 mm wide respectively. Thus, each of the paddles may be rotated  $12^\circ$  with respect to the paddle that preceded it so that they form a cylindrical shape with a conical end. This geometrical design for the ST increases solid angle coverage while minimizing multiple scattering.

### 1.3. Support Structure

The ST scintillator paddles are placed atop a low density Rohacell ( $\rho = 0.075 \text{ g/cm}^3$ ) foam support structure which envelopes the target vacuum chamber seen in Fig. 4. The Rohacell, which is 11 mm thick, is rigidly attached to the upstream support chassis and extends down the length of paddles however, not to include the last few centimeters of the conical nose section. Glued to the inner dia-

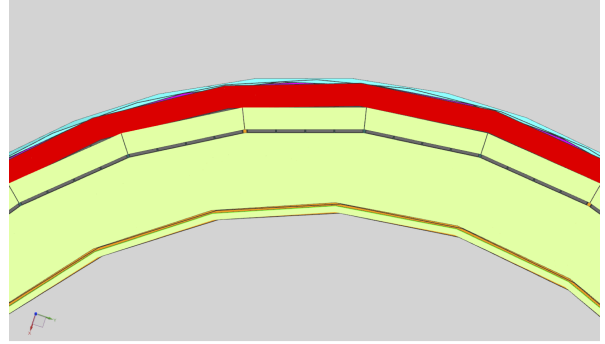


Figure 5: Composition of the Start Counter Materials.

ter of the Rohacell support structure are 3 layers of carbon fiber ( $\rho = 1.523 \text{ g/cm}^3$ ) each of which are  $650 \mu\text{m}$  thick. A cross section of the ST can be seen in Fig. 4 where the carbon fiber is visible. The carbon fiber provides additional support during the assembly process as well as long term rigidity.

The various layers of material that comprise the ST support structure is illustrated in Fig. 5. In order to ensure that the detector was light-tight, a plastic collar was placed around the top of the SiPMs at the upstream end as seen in Fig. 5. The

collar served as a lip to which a cylindrical sheet of black Tedlar was taped too. At the tip of the nose, a cone of Tedlar was then connected to the aforementioned cylindrical section. To make the downstream end of the ST light-tight, another cone of Tedlar was taped to the nose of the inner Rohacell support structure and then attached to the top Tedlar cone layer.

#### 1.4. SiPM Readout Detectors

The selected readout for each scintillator bar is the magnetic field insensitive Hamamatsu S10931-050P surface mounted Multi-Pixel Photon Counters (MPPCs)[6]. An individual  $3 \times 3 \text{ mm}^2$  MPPC, also known as a SiPM, in the aforementioned configuration is comprised of 3600 individual,  $50 \times 50 \mu\text{m}^2$ , Avalanche Photo-Diode (APD) pixel counters operating in Geiger mode. The signal output from each SiPM is the total sum of the outputs from all 3600 APD pixels[7]. The scintillation light from an individual scintillator bar is collected by an array of four of these SiPMs.

The SiPM readout detectors are housed in a ceramic case which is surface mounted to a custom fabricated Printed Circuit Board (PCB). The PCB is held in a fixed position while being attached to the lip of the upstream chassis *via* two screws as illustrated in Fig. 6. The individual ST scintillators are coupled *via* an air gap ( $< 250 \mu\text{m}$ ) to groups of four SiPMs set in a circular arrangement as can be seen in Fig. 6.

#### 1.5. Readout Electronics

The SiPMs reading out one individual paddle, are current summed prior to pre-amplification. The



Figure 6: ST1 of Start Counter read out system. The ST1's are rigidly attached to the upstream support chassis. Approximately 72% of the scintillator light is collected at the upstream end.

output of each preamp is then split; buffered for the Analog to Digital Converter (ADC) output, and amplified for the Time to Digital Converter (TDC) output by a factor five relative to the ADC. The ADC outputs are readout *via* JLab VME64x 250 MHz Flash ADC modules while the TDC outputs are input into JLab leading edge discriminators, followed by a high resolution 32 channel JLab VME64x F1TDC V2 module. Furthermore, each group of four SiPMs utilizes a thermocouple for temperature monitoring. There are 120 SiPMs in total, for a total of 30 pre-amplifier channels as seen Fig. 7.

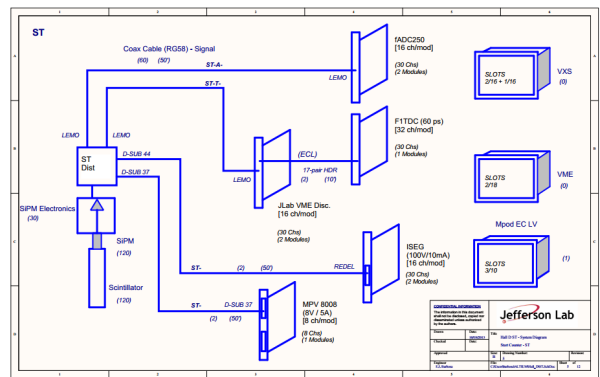


Figure 7: Start counter readout electronics diagram.

There are three components that comprise the

<sup>140</sup> ST detector readout system. The first component is the ST1 which holds 3 groups of 4 SiPMs as can be seen in Fig. 6. In order to mimic the geometry of the 30 paddle design one group of SiPM's is rotated by  $12^\circ$  relative to the central group, while  
<sup>145</sup> the other adjacent group is rotated by  $-12^\circ$ . One ST1 unit will collect light from three paddles individually. The ST1 implements the current sum and bias distribution per group of 4 SiPMs. It also has a thermocouple for temperature monitoring.

<sup>150</sup> The second component is the ST2, seen in Fig. 8, is a Printed Circuit Board (PCB) that houses the signal processing electronics of the readout system.  
<sup>165</sup> It has 3 channels of pre-amplifiers, 3 buffers, and



Figure 8: Fully assembled ST readout system.

<sup>155</sup> 3 factor five amplifiers. Furthermore, it has 3 bias distribution channels with individual temperature compensation *via* thermistors. The ST2 is attached to the ST1 *via*  $90^\circ$  hermaphroditic connector.

<sup>160</sup> The third component of the readout system, the ST3 seen in Fig. 9, provides interface to the power and bias supplies. It also routes the ADC and TDC outputs as well as the thermocouple output. The



Figure 9: Start counter ST3 readout system.

ST3 connects to the ST2 *via* a signal cable assembly seen in Fig. 8 and Fig. 9. The ST3 is installed upstream of the Start Counter and next to the beam pipe.

## 2. GEANT4 Simulations

In this section, the Monte Carlo (MC) simulations that were conducted in order to better understand the performance and characteristics of scintillators machined to the nominal GLUEX Start Counter design are discussed. Comparisons were made with the data observed in experiments conducted on the bench. The MC studies were performed with the use of the simulation tool-kit GEANT4 which simulates the passage of particles through and interacting with matter [8].

### 2.1. Simulating a Simplified Model of the ST

As discussed in Sec. 1.2, the ST scintillator paddles have a unique geometry in which the nose section tapers in width as the paddles approach the beam line. This tapering effect results in a unique phenomenon in which the light output of the scintillator paddle begins to increase as the source moves further away from the readout detector. At first,

185 this phenomenon is completely contrary to what  
one might expect. When the source moves fur-  
ther away from the end being readout, the photons  
have a larger effective path length and thus, have  
an increased probability in being lost for detection.  
190 However, this is antithetical relative to what is ob-  
served.

A primitive GEANT4 simulation was conducted  
to investigate the aforementioned phenomenon. For  
simplicity, only the two trapezoidal regions of a ma-  
195 chined scintillator paddle were considered. Namely,  
the wide straight section and the tapered nose sec-  
tion which are illustrated in the GEANT4 event  
display seen in Fig. 10.

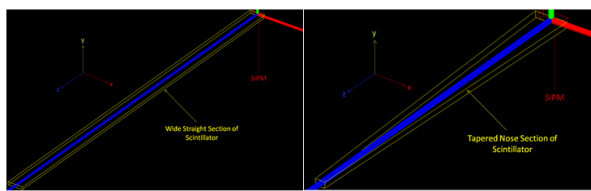


Figure 10: Simulated straight & nose section geometries. Shown is the GEANT4 event display. Left: wide straight section. Right: tapered nose section. The sections have been oriented such that they are in the same coordinate system as defined in HallD. The yellow lines are the scintillator boundaries, while the red lines are the boundaries of the SiPM.

The EJ-200 scintillator material ( $\rho =$   
200  $1.023 \text{ g/cc}^3$ ,  $n = 1.58$ ) [3] was simulated with  
only one free parameter utilized to characterize  
the scintillator bar *i.e.*, the reflectivity of the  
*G4LogicalSkinSurface*, was set to 98% so there  
remained some finite probability that photons  
205 could be lost in the scintillator medium. Furthermore,  
the SiPM readout detector was placed at  
the upstream end of the two sections, seen in Fig.

10. Moreover, the SiPM was constructed as a  
*G4SensitiveDetector* made of Silicon with a 100%  
210 detection efficiency. The SiPM was constructed  
to have an active area of  $3 \times 12 \text{ mm}^2$  which is identical to the readout system described in  
Sec. 1.4.

In order to simulate a charged particle traversing  
through the scintillator medium resulting in the  
production of photons along its path through the  
material, optical photons were generated inside the  
volume of the simulated scintillator material. The  
scintillation yield was defined to be  $10,000\gamma/\text{s}/1$   
215 MeV [3]. For visual purposes, Fig. 11 shows 100  
optical photons being produced at the tip of the far  
end of the two sections of the simulated scintillator  
paddle.

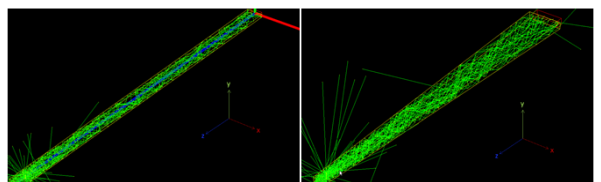


Figure 11: 100 Optical photons generated in the straight & nose sections. Left: wide straight section. Right: tapered nose section. The neon green lines are the paths of the optical photons. It is clear that some photons do in fact escape the scintillator medium, while others are collected in the simulated SiPM detector.

In order to sample the entirety of the two sections, 10,000 optical photons were generated at 16 different locations inside the medium of the scintillator. The photon energies ranged between 0.5–3.0 eV [9] and were generated randomly in  $4\pi$  along a 3 mm path ( $y - axis$ ) in the scintillator medium. The path was oriented orthogonal to the wide surface of the scintillator. In essence, this simulates

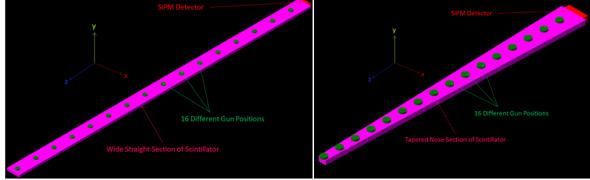


Figure 12: Optical photon gun locations along the straight & nose sections. Left: wide straight section. Right: tapered nose section. The magenta geometries indicate the scintillator boundaries of the two sections. The red box is the sensitive SiPM detector, and the green cylinders represent the location of the 16 optical photon gun locations. The locations of the source were chosen to be equal distances apart relative to each of the two sections.

a charged particle traversing through the medium with a  $\theta_{track} = 90^\circ$  in hall coordinates. The number of photons collected by the SiPM at each of the 16 source locations is counted and correlated to the source location. The results can be seen in Fig. 13. From the data it is clear that the geom-

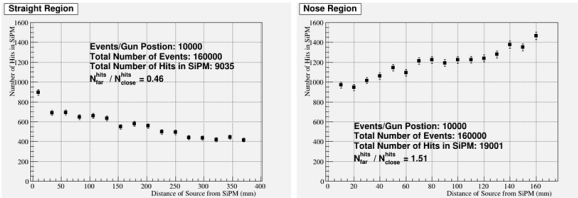


Figure 13: Simulation results for simplified two section scenario. The total number of photons which were collected by the SiPM detector at each of the 16 source locations is plotted against the sources distance from the sensitive detector. Left: wide straight section. Right: tapered nose section.

etry of the nose section results in an improvement of light collection as the source moves further away from the readout detector. In fact, there is a factor  $\approx 1/2$  light loss observed in the straight section upon comparing the number of hits collected at the closest and furthest locations relative to the readout detector. However, there is factor  $\approx 3/2$  light

gain observed in the nose region. These results are primarily due to the unique scintillator geometry. This phenomenon is advantageous in the case of the ST since the majority of forward going charged particles will traverse through the nose region.

## 2.2. Simulating Machined Scintillator Geometry

Further simulations were conducted to simulate more realistically the effects of light collection that results from the ST scintillator geometry and optical surface quality. The ST scintillator geometry was imported into GEANT4 from a Vectorworks CAD drawing utilizing the CADMesh utility [10] and is shown via the GEANT4 event display in Fig. 14. The SiPM was constructed as

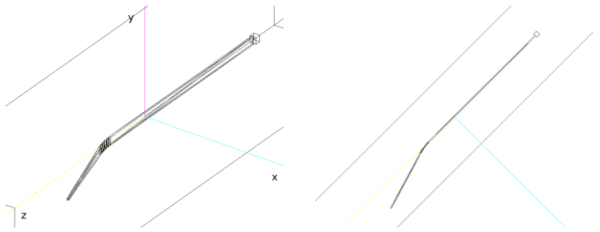


Figure 14: Scintillator geometry imported into GEANT4 utilizing CADMesh Utility. The scintillator is coupled to a SiPM detector. Left: isometric view. Right: top view. The tapering of the nose section is clearly visible.

a  $12 \times 12 \times 10$  mm $^3$  volume with a  $100 \mu\text{m}$  air gap between it and the wide end of the straight section. Furthermore, the volume surrounding the scintillator volume was air. The EJ-200 scintillator material, SiPM silicon detector, and optical photons were defined in an identical manner discussed in Sec. 2.1.

To simulate the imperfections of the scintillator surfaces due to manufacturing and machining, an optical surface “skin” was defined. The “skin” ma-

terial was defined to be of they type “dielectric-dielectric” and made use of the UNIFIED physics model [11] to define an imperfect scintillator surface. Both the transmission efficiency and reflection parameters were implemented as free parameters to study their various effects on light transmission..

The UNIFIED model allows one to define the finish of the scintillator surface as *polished*, *ground*, or *unified* and is illustrated in Fig. 15 [11].

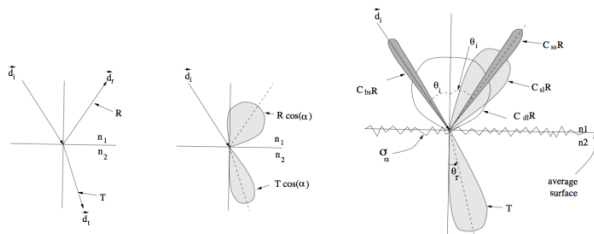


Figure 15: UNIFIED Model of scintillator surfaces. Left: Polar plot of the radiant intensity of the polished (left) and ground (right) models. Right: Polar plot of the radiant intensity in the UNIFIED model.

In the polished model, Fresnel reflection and refraction is assumed, where as the ground model allows for Lambertian reflection, Fresnel refraction, backscattering, as well as spike and lobe reflections. The spike ( $C_{ss}$ ) reflection parameter assumes the optical photons are reflected as if the surface was a perfect mirror. The backscattering ( $C_{bs}$ ) reflection parameter assumes the photon is reflected in the same direction of incidence. The Lambertian ( $C_{dl}$ ) reflection parameter assumes that the photons are reflected corresponding to a Lambertian distribution. The lobe ( $C_{sl}$ ) reflection parameter assumes that the photons will reflect based on the orientation of the micro-facet on the scintillator surface, where  $\sigma_\alpha$  defined the standard deviation of the distribution of the micro-facets orientation [11]. One

caveat of the aforementioned models is that they assume identical parameters for the entire optical surface [12].

As was done in section 2.1 10,000 optical photons were generated in the scintillator medium every 2.5 cm and the number of hits collected in the SiPM were recorded. The results of these simulations are show in Fig. 16. It is clear that while assuming a

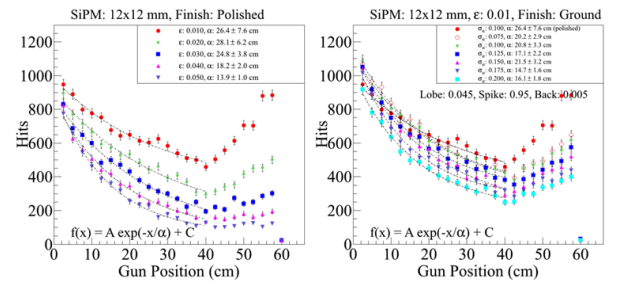


Figure 16: UNIFIED Model results. Left: polished model while varying the transmission efficiency. Right: ground model with varying  $\sigma_\alpha$  which characterizes the standard deviation of the surfaces micro-facet orientation.

polished surface and the transmission efficiency is increased, the amount of light collected in the SiPM also increases. This is illustrated in Fig. 16. Similarly, as the number of micro-facet orientations increase, meaning a more coarsely ground surface, the amount of light collection in the SiPM decreases as expected. Moreover, in the instances where the surface quality of the machined scintillators are good, the phenomenon of light increase in the nose region as the source moves further from the readout detector is clearly observed.

### 3. Misalignment Studies

To protect both the active area of the SiPMs and the scintillator surface at the upstream end of the straight section, the coupling distance between

the two was required to be larger than zero. Similarly, the scintillator paddles were also shimmed radially such that the top edge of the scintillator was level with the top edge of the active area of the SiPM thereby maximizing light collection. It was therefore necessary to study the effects of SiPM/scintillator misalignments on light collection and time resolution.

The SiPM sits atop a Newport MT-XYZ (MT) compact dovetail XYZ linear translation stage with three fine adjustment screws with 80 threads per inch as seen in Fig. 17. Each translation knob for

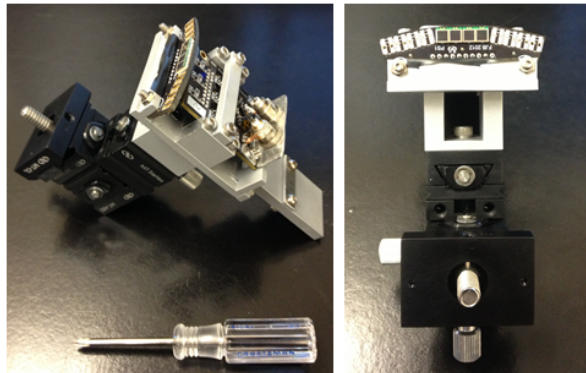


Figure 17: The SiPM case is the aluminum matt finished metal. The translation stage is black. Left: isometric view of SiPM case and MT-XYZ translation stage. Right: front view (looking upstream).

the three axes of translation provides a translation of  $318 \mu\text{m}$  per rotation. It is useful to note that for each location of the SiPM, relative to the scintillator, the source and trigger PMT were located at  $z = 24.467 \text{ cm}$  and 10,000 event triggers were collected.

### 3.1. Vertical Alignment of SiPM & Scintillator

To study the effects of the various horizontal (translations along the  $z$ -axis) coupling distances,

the relative position of the active area of the SiPM and the top edge of the scintillator paddle was required to be known. Vertical alignment is the most critical since the 3 mm thickness of the scintillator matches the 3 mm height of the active area of the SiPM. To test the 50 machined scintillators in a reproducible manner, the vertical alignment of the SiPM and scintillator must be replicated in a robust manner.

Utilizing an Edmund Optics CMOS camera, and a ruler (seen in Fig. 18) the vertical alignment of the top edges of the SiPM and scintillators could be measured within 0.025 mm accuracy relative to the ST2 PCB Board. The  $3 \times 3 \text{ mm}^2$  SiPMs, which

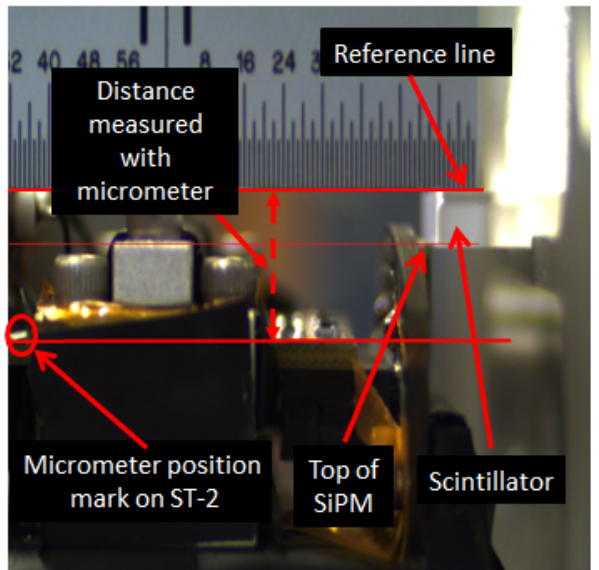
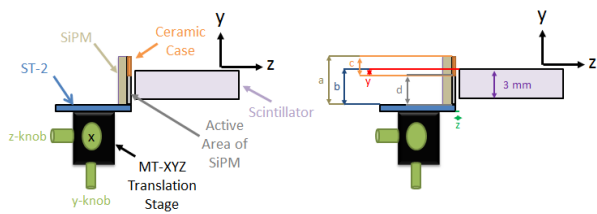


Figure 18: Vertical alignment optics set-up. The reference line corresponds to the top surface of the scintillator, while the micrometer position on the ST2 is clearly marked so that the absolute difference could be measured both optically and manually with a micrometer.

are mounted to the ST1, are housed in a ceramic case mounted on the ST1 PCB. Therefore, there exists some area between the top of the SiPM ce-

355 ceramic case and the active area of the SiPM which must be taken into account. The distance is also measured both optically and manually relative to the ST2 PCB.

360 Figure 19 illustrates a labelled schematic similar to what was seen in Fig. 18 and depicts the variables measured and monitored so as to quantify the vertical alignment. Of all the variables in Fig. 19,  $y$



380 Figure 19: Vertical alignment optics schematic. Left: labelled cartoon of SiPM & scintillator vertical alignment. Right: variables used to quantify vertical alignment. The scintillator is intentionally misaligned in this cartoon so that the misalignment parameter  $y$  is visible.

365 is of the utmost importance since it is the distance between the top edge of the scintillator paddle and the active area of the SiPM and is the quantization of the vertical misalignment. That is to say the at  $y = 0$  the SiPM and scintillator are aligned vertically. Both the distance between the top of the SiPM and ST2 PCB ( $a$ ), and the distance between the top of the SiPM and the active area of the SiPM ( $c$ ), are measured optically and define the distance between the top edge of the active area of the SiPM and the ST2 PCB ( $d$ ) via  $d = a - c$ , which are all constants. It is necessary to note that 370 the coupling distance between the active area of the SiPM and scintillator ( $z$ ) was done by eye and then measured optically until a desirable coupling distance was found. The values of the aforementioned

variables are summarized in Table 1. The variable

| Variable | Value (mm) |
|----------|------------|
| $a$      | 5.22       |
| $c$      | 0.91       |
| $d$      | 4.32       |
| $z$      | 0.25       |

Table 1: Vertical alignment variables. All variables were measured five times and the numbers reported are averages of those values.

385  $b$  defines the distance between the top edge of the scintillator and the ST2 PCB and is measured both optically and manually. This distance, coupled with the constant  $d$ , provides the measured quantity  $y$  through the difference  $y = b - d$ .

The coordinate system used to quantify the vertical misalignment studies is illustrated in Fig. 20. The scintillator remained fixed, while the SiPM was

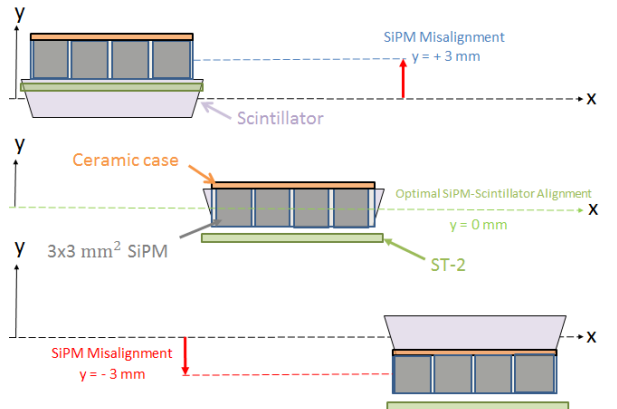


Figure 20: Vertical alignment schematic. The scintillator is fixed while the SiPM effectively scans across the face of the scintillator along the  $y$ -axis.

lowered, relative to the scintillator, to the minimum location governed by the range of the MT translation stage at approximately  $y = -4 \text{ mm}$ . Coarse measurements were then taken at half turns

( $159 \mu\text{m}$ ) intervals until the maximum height of the MT translation stage was reached which was approximately  $y = +4 \text{ mm}$ . The results of these measurements can be seen in Fig. 21. Once the

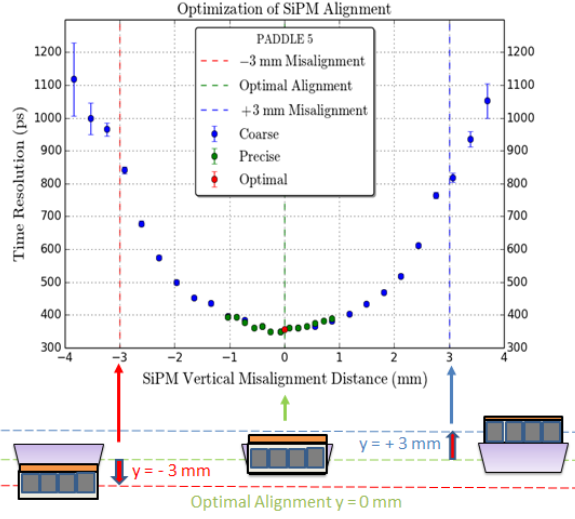


Figure 21: Coarse vertical misalignment results. The minimum time resolution obtained was approximately 350 ps which was expected. Once the SiPM exceeded  $y = \pm 3 \text{ mm}$  there is no active area of the SiPM coupled to the face of the scintillator.

395 coarse measurements concluded, the SiPM was lowered to  $y \approx -1 \text{ mm}$  and then the translation stage  
 400 was moved in quarter turn ( $79.5 \mu\text{m}$ ) intervals until  $y \approx +1 \text{ mm}$  was reached. The results of both the coarse and fine measurements are seen in Fig. 22. It is useful to note that at every location of the SiPM the distance traversed was verified by a manual measurement made with a micrometer (1 mil precision).

405 From the vertical misalignment studies it is clear that there is no significant variation of time resolution within a  $\pm 300 \mu\text{m}$  range of the ideal alignment. These results were also simulated in a manner similar to what was discussed in section ?? and the

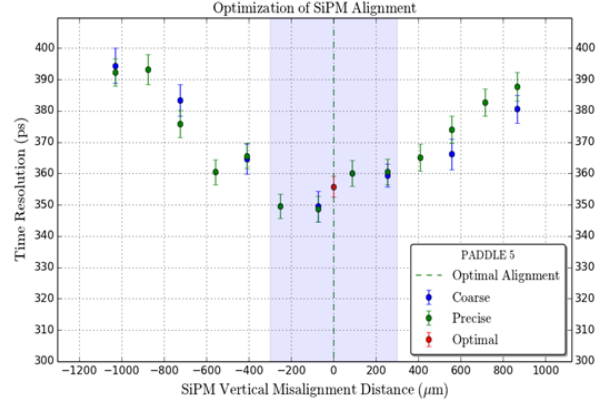


Figure 22: Fine vertical misalignment results. Note that the coarse and fine measurements were overlapped so the reproducibility of the measurements were depicted.

results are seen in Fig. 23. The Geant4 simulations

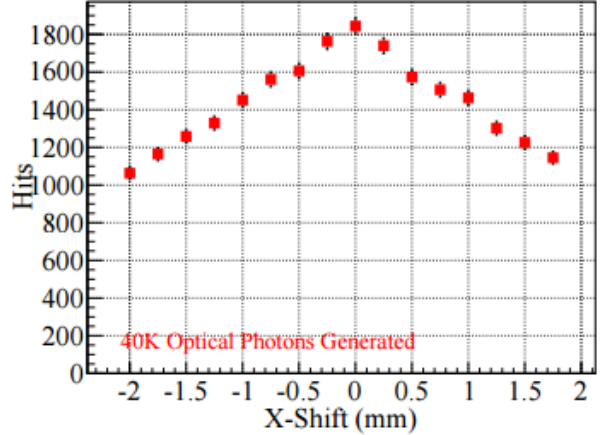


Figure 23: Vertical alignment simulation studies [13]. It is important to note the x-axis corresponds to the y-axis as discussed with the experimental measurements.

410 indicate that the acceptable range of vertical misalignment is approximately  $\pm 250 \mu\text{m}$  [13] which is consistent with what was measured on the bench at FIU.

### 3.2. Coupling Distance of SiPM & Scintillator

With the vertical alignment between the scintillator and SiPM optimized, the effects of varying

the coupling distance was studied. Using an identical set-up as was described in section 3.1 the coupling distance, and resulting time resolutions, was measured at various locations with three distances shown in Fig. 24. While the coupling distance was

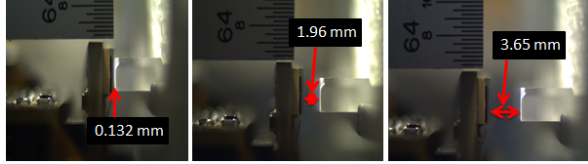


Figure 24: Coupling distance optics. Various coupling distances as measured with the CMOS camera. The high degree of precision is clearly visible.

varied, the vertical alignment was kept constant at the optimal location determined from the studies outlined in section 3.1 and was monitored both optically and manually.

With the optimal vertical alignment having been verified, the SiPM was moved *via* the MT translation stage along the  $z - axis$  such that the active area of the SiPM was flush against the face of the machined scintillator paddle at  $z = 0$  mm. In the coupling region  $z < 1$  mm the SiPM was receded from the face of the SiPM in  $1/4$  turn ( $79.5 \mu\text{m}$ ) intervals. For  $1 \text{ mm} < z < 2 \text{ mm}$ , the SiPM was receded from the face of the SiPM in  $1/2$  turn ( $159 \mu\text{m}$ ) intervals, and for  $2 \text{ mm} < z < 4 \text{ mm}$  data were collected in 1 turn ( $318 \mu\text{m}$ ) intervals and is illustrated in Fig. 25.

Figure 26 zooms in on the ( $z < 1$  mm) region of the coupling distance studies shown in Fig. 25. It is clear from the data the optimal coupling range was  $50 \mu\text{m} < z < 350 \mu\text{m}$  and there was no significant reduction in time resolution performance over a  $0 \mu\text{m} < z < 600 \mu\text{m}$  range. Similarly,

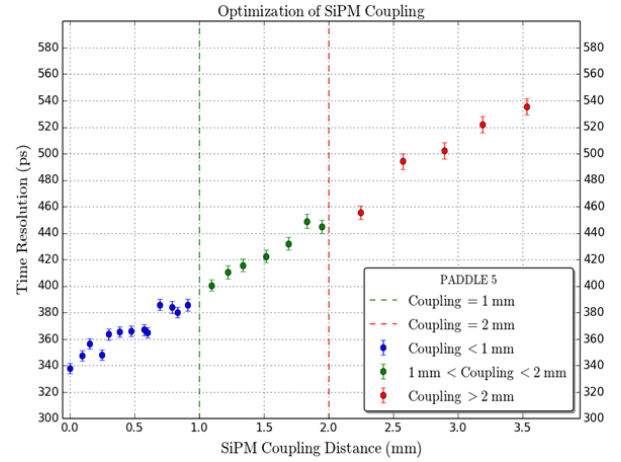


Figure 25: Coarse coupling distance studies. It is useful to note that at a coupling distance of  $251 \mu\text{m}$  the time resolution was identical to what was measured in Fig. 22 while conducting the vertical alignment studies.

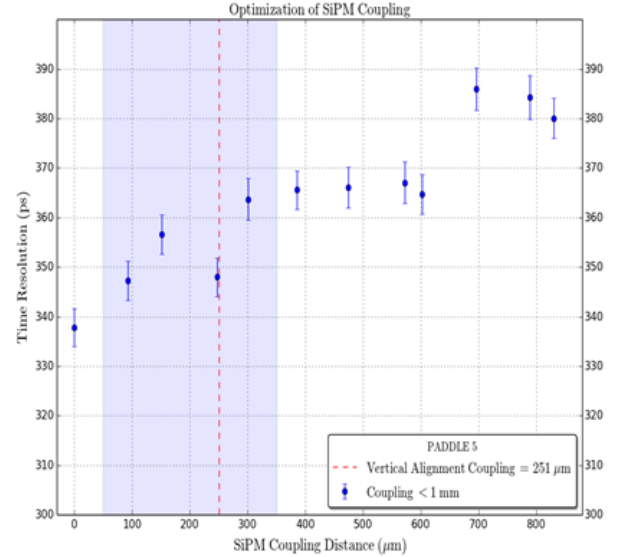


Figure 26: Fine coupling distance studies. The blue shaded region ( $50 \mu\text{m} < z < 350 \mu\text{m}$ ) indicates the optimal coupling range.

the simulation results also indicate that there is no significant reduction in light collection in the  $0 \mu\text{m} < z < 600 \mu\text{m}$  range [13].

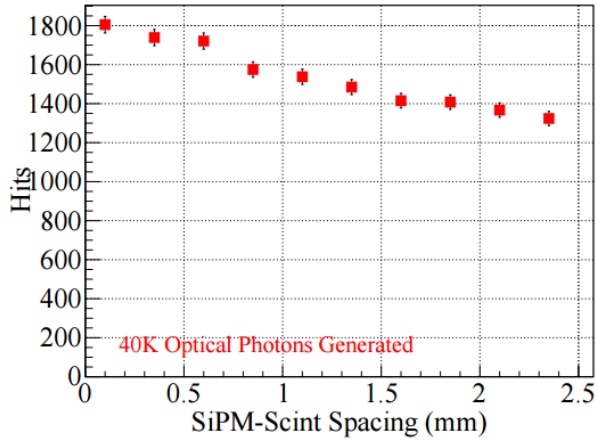


Figure 27: Coupling distance simulations. Simulations indicated that the optimal coupling distance is in the  $50 \mu\text{m} < z < 350 \mu\text{m}$  range.

#### 4. Fabrication

In order to successfully identify the 2 ns electron beam bunch structure delivered by the CEBAF to within 99% accuracy, the GLUEX Start Counter time resolution is required to be  $< 350 \text{ ps}$ . In the following section the details of polishing and characterizing machined scintillators, as well as the construction of the Start Counter are discussed.

##### 4.1. Polishing Machined Scintillators

The surfaces of the machined scintillators incurred a plethora of surface defects and chemical contaminants known to harm scintillator surfaces while undergoing edge polishing at McNeal Enterprises. Therefore, in an effort to recover the scintillator surfaces and performance capabilities, polishing was required.

Prior to polishing the machined scintillators, a coarse measurement of the paddles performance was conducted to understand the magnitude of damage the paddles had incurred, relative to pro-

totypes, as a result of mishandling. The time resolution and light output was measured at three precise locations along the length of the scintillators. One measurement was taken in the middle of the straight section, one in the middle of the bend, and one at the tip of the nose.

Figure 28 illustrates the erratic fluctuation and poor performance that existed from paddle to paddle prior to polishing. On average the 50 paddles

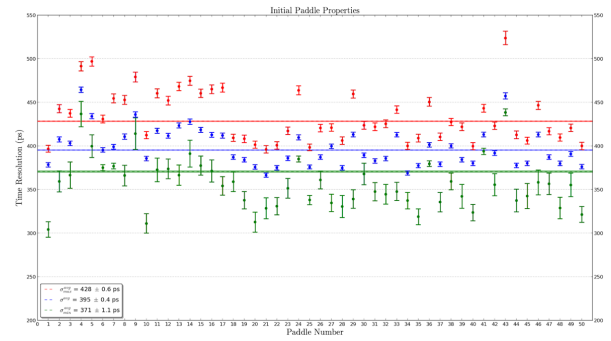


Figure 28: Coarse time resolution measurements prior to polishing. Paddle number is on the x-axis and time resolution in ns is on the y-axis. The red points are the resolutions in the bend region, the blue points are the weighted average of the three measurements, and the green points are the resolutions at the tip of the nose. The horizontal lines are the weighted averages of the individual measurements.

did not meet the design resolution of 350 ps.

To polish the machined scintillator surfaces, Buehler Micropolish II deagglomerated  $0.3 \mu\text{m}$  alumina suspension was utilized[14]. The polishing suspension was diluted with a 5:1 ratio of de-ionized  $\text{H}_2\text{O}$  to alumina and applied to a cold, wet  $6'' \times 0.5''$  Caswell Canton flannel buffering wheel[15] operated at  $< 1500 \text{ RPMs}$ . All surfaces of the scintillators were carefully buffed until all large, uniform surface defects were removed. In order to eliminate small, localized surface defects hand polishing with

a soft NOVUS premium Polish Mate microfilament cloth[16] and diluted polishing suspension was applied. These polishing procedures made the scintillators void of virtually all scratches and surface defects.

Once the appropriate polishing procedures had been developed and implemented the surface quality was greatly improved as can be seen in Fig. 29 which illustrates the same scintillator paddle before and after polishing. A red laser beam was shone

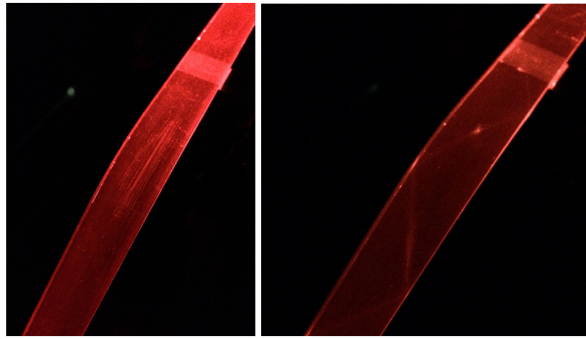


Figure 29: Effects of polishing scintillators. Left: non-diffuse laser incident on an edge, before polishing, at the upstream end of the straight section. Right: non-diffuse laser incident on the same edge, after polishing, at the upstream end of the straight section.

into the scintillator medium from the upstream end aimed at one edge so that the total internal reflection towards the tip of the nose was visible. The unpolished scintillator had such poor surface quality that the reflections in the bend region could not be seen due to the multiple scattering of light at the scintillator boundaries. However, the reflections in the polished scintillator can clearly be seen traversing down through the nose region.

Once the scintillators were polished, their performance was remeasured so that a quantitative measure of the polishing effects were understood. The

measurements were performed in an identical manner outlined above and the pre-polished results were illustrated in Fig. 28. As expected, the time resolutions were greatly improved as seen in Fig. 30. On average, at the tip of the nose, the scintillators

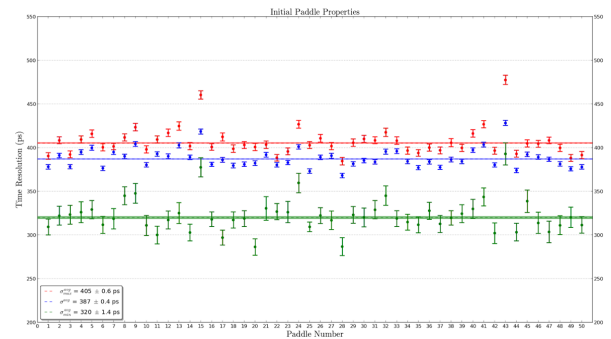


Figure 30: Coarse time resolution measurements after polishing. The details are identical to Fig. 28

exhibited a  $\approx 15\%$  improvement in time resolution. Moreover, there was a substantial reduction in erratic fluctuations in performance.

#### 4.2. Testing Machined Scintillators

The polished machined scintillators were tested in order to measure their light output and time resolution properties. They were measured in an identical and reproducible manner utilizing a custom fabricated test stand shown in Fig. 31. The test

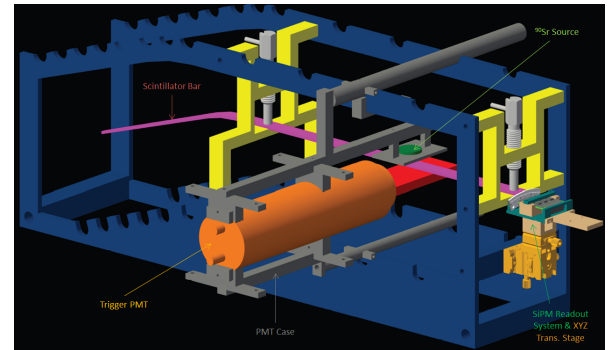


Figure 31: CAD Drawing of custom test stand.

stand facilitated the precise measurement of the  
 525 aforementioned scintillator properties at 12 well-defined locations along the length of the scintillator paddles. Specifically 4 locations in the straight section, 3 in the bend, and 5 in the nose were tested.

The measurements were conducted with a collimated  $^{90}\text{Sr}$  source oriented orthogonal to the wide flat surface of the scintillators. The  $^{90}\text{Sr}$  source provided minimum ionizing electrons ranging in energy from 0.5 – 2.3 MeV *via* beta-decay [17][18]. A trigger Photo-Multiplier Tube (PMT) was placed underneath the scintillator on the opposite side of the  
 535  $^{90}\text{Sr}$  source and provided the TDC start time and ADC gate. A prototype SiPM detector identical to the SiPMs installed in the final ST assembly, was utilized to collect the light from the scintillators.  
 540

The analog signals from the SiPM and the trigger PMT were then processed through Nuclear Instrumentation Modules (NIM) so that both the ADC and TDC spectra could be analyzed. The signal processing electronics diagram is illustrated in  
 555 Fig. 32.

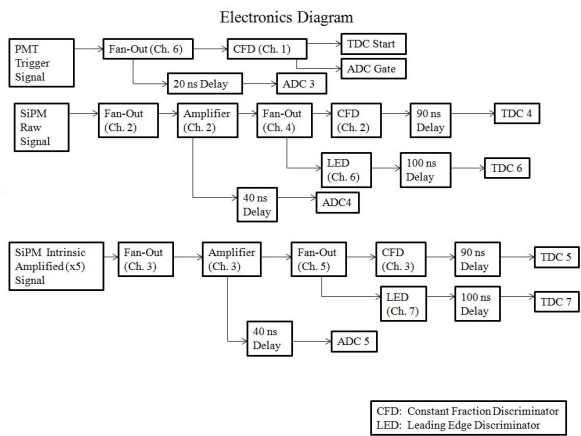


Figure 32: Electronics diagram for testing machined scintillators.

Utilizing a dedicated data acquisition computer configured with CEBAF Online Data Acquisition (CODA) software, 10,000 event triggers and associated data were collected at each of the locations along the scintillator path. Subsequently, the ADC and TDC data were analyzed to measure the light output and time resolutions respectively of the whole lot of polished machined scintillators.

Once the 30 machined scintillator paddles which exhibited the best time resolution and light output properties from the lot of 50 were selected, they were carefully wrapped in Reynolds food grade aluminum foil. The aluminum foil is  $16.5 \mu\text{m}$  thick and possesses good reflectivity properties. Moreover, the aluminum foil protects the surfaces of the scintillators during both the testing and assembly processes.

The measured time resolutions for the 30 best scintillators, which comprise the ST, were found to be satisfactory and even well below design resolution in the nose region which is illustrated in Fig. ??.

The unique geometry of the machined scintillator paddles exhibit a phenomenon of an increase in light collection in the nose region as the light source moves towards the tip at the downstream end. It is hypothesized that the relatively poor time resolution in the straight section is due to a reflective smearing effect in which light is able to traverse from the straight section down to the tip of the nose, and then back up to the upstream end.

The average time resolution of the individual scintillators selected for the final ST assembly are shown in Fig. ??.

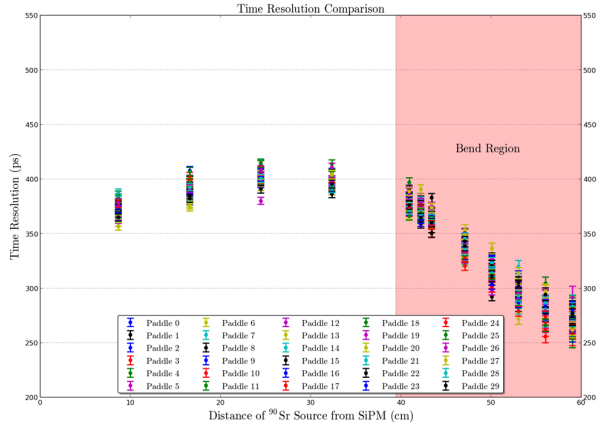


Figure 33: Time resolution of 30 the best scintillator paddles. The time resolution performance of the selected scintillators is remarkably similar while illustrating a spread of  $\approx 50$  ps in the nose region.

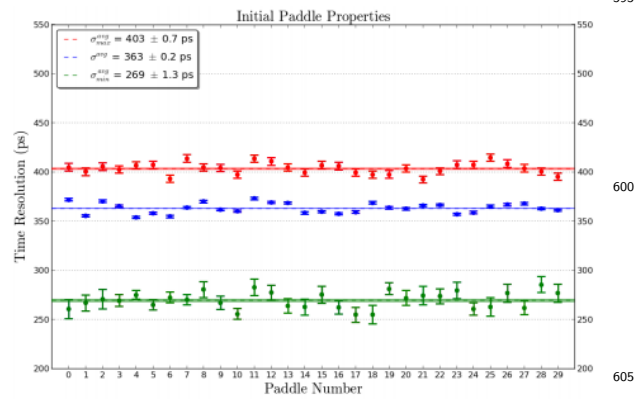


Figure 34: Average time resolution of 30 best scintillator paddles. The red data points correspond to the maximum time resolution obtained in all 12 data points. The blue data points are the weighted average of all 12 data points. The green data points indicate the minimum time resolution obtained in all 12 data points.

#### 4.3. Assembly

## References

- [1] E. Pooser, The GlueX start counter and beam asymmetry  $\Sigma$  in single  $\pi^0$  photoproduction, Ph.D. thesis, Florida International University (2016).
- [2] <http://www.eljentechnology.com/>.
- [3] General Purpose Plastic Scintillator EJ-200, EJ-204, EJ-208, EJ-212, technical note available at [http://www.eljentechnology.com/images/products/data\\_sheets/EJ-200\\_EJ-204\\_EJ-208\\_EJ-212.pdf](http://www.eljentechnology.com/images/products/data_sheets/EJ-200_EJ-204_EJ-208_EJ-212.pdf).
- [4] <http://www.rohacell.com>.
- [5] <http://www.mcnealplasticmachining.com/>.
- [6] <http://www.hamamatsu.com/us/en/index.html>.
- [7] Multi-Pixel Photon Counter, technical note available at [https://halldweb1.jlab.org/wiki/images/4/49/S10362-33\\_series\\_kapd1023e05.pdf](https://halldweb1.jlab.org/wiki/images/4/49/S10362-33_series_kapd1023e05.pdf).
- [8] <https://geant4.web.cern.ch/geant4/>.
- [9] K. S. Krane, Introductory Nuclear Physics, John Wiley & Sons, 1988, Ch. Detecting Nuclear Radiations, pp. 201–202.
- [10] C. M. Poole, A cad interface for geant4, paper submitted to Cornell Archive (arXiv) May 5, 2011 (2011). URL <http://arxiv.org/pdf/1105.0963.pdf>
- [11] A. L. . C. Moison, A more physical approach to model the surface treatment of scintillation counters and its implementation into detect, paper presented at IEEE, Nuclear Science Symposium; Anaheim, November 2-4 available at <http://geant4.slac.stanford.edu/UsersWorkshop/PDF/Peter/moisan.pdf> (1996).
- [12] P. Khetarpal, Start Counter Geant4 Simulations, start Counter Geant4 Simulations Wiki available at [https://halldweb.jlab.org/wiki/index.php/Start\\_Counter\\_Simulations](https://halldweb.jlab.org/wiki/index.php/Start_Counter_Simulations).
- [13] P. Khetarpal, Start counter: Optics simulations, talk Given at the February 16, 2012 GlueX Collaboration meeting (2012). URL [http://argus.phys.uregina.ca/gluex/DocDB/0019/001921/002/khetarpal\\_feb2012.pdf](http://argus.phys.uregina.ca/gluex/DocDB/0019/001921/002/khetarpal_feb2012.pdf)
- [14] <https://shop.buehler.com/consumables/grinding-polishing/polishing-suspensions/alumina-suspensions>.
- [15] <http://www.caswellplating.com/buffing-polishing/buffing-wheels/canton-flannel-wheels.html#>.

- [16] [https://www.novuspolish.com/polish\\_mates.html](https://www.novuspolish.com/polish_mates.html).
- [17]  $^{90}\text{Sr}$  Decay Radiation Data, national Nuclear Data  
625 Center, Nuclear Structure and Decay Database  
(NuDat) available at <http://www.nndc.bnl.gov/nudat2/decaysearchdirect.jsp?nuc=90SR&unc=nds>.
- [18]  $^{90}\text{Y}$  Decay Radiation Data, national Nuclear Data  
Center, Nuclear Structure and Decay Database  
630 (NuDat) available at <http://www.nndc.bnl.gov/nudat2/decaysearchdirect.jsp?nuc=90Y&unc=nds>.